

Algebraic language models for inverse design of metamaterials via diffusion transformers

Received: 30 July 2025

Accepted: 10 March 2026

Published online: 23 April 2026

 Check for updates

Li Zheng¹, Siddhant Kumar²✉ & Dennis M. Kochmann¹✉

Generative machine learning models have revolutionized material discovery by capturing complex structure–property relationships, yet extending these approaches to the inverse design of three-dimensional metamaterials remains limited by computational complexity and underexplored design spaces due to the lack of expressive representations. Here we present DiffuMeta, a generative framework integrating diffusion transformers with an algebraic language representation, encoding three-dimensional geometries as mathematical sentences. This compact, unified parameterization spans diverse topologies, enabling the direct application of transformers to structural design. DiffuMeta leverages diffusion models to generate new shell structures with precisely targeted stress–strain responses under large deformations, accounting for buckling and contact while addressing the inherent one-to-many mapping by producing diverse solutions. Uniquely, our approach enables simultaneous control over multiple mechanical objectives, including linear and nonlinear responses beyond training domains. Experimental validation of fabricated structures further confirms the efficacy of our approach for accelerated design of metamaterials and structures with tailored properties.

Recent advances in additive manufacturing have enabled precise fabrication of architected (meta-)materials with unprecedented control over their properties by leveraging carefully engineered architectures across multiple length scales^{1,2}. Among the various classes of metamaterials, shell networks^{3,4} have attracted particular interest due to their exceptional stiffness-to-weight ratio⁵ and superior energy absorption⁶. Unlike beam-based or plate-based lattices that exhibit stress concentrations at discrete junctions^{7,8}, shell lattices use continuous, smoothly curved surfaces to distribute loads effectively, enabling enhanced load-bearing capability and resistance to global buckling⁹. These mechanical advantages, coupled with their highly tunable topologies, position shell lattices as ideal candidates for applications including heat exchangers¹⁰, soft robotics¹¹ and energy-absorbing components¹².

To fully harness the design potential of architected materials, considerable efforts have focused on the inverse design problem: identifying small-scale structures that achieve specified effective target properties. This challenge has been primarily addressed through

topology optimization^{13,14}, which, however, requires extensive forward finite element (FE) simulations, posing substantial challenges for high-dimensional design spaces and nonlinear target properties. More recently, data-driven machine learning approaches have emerged as promising alternatives, with surrogate models providing fast property predictions^{15,16} and deep generative models—such as variational autoencoders¹⁷ and generative adversarial networks¹⁸—demonstrating remarkable success in materials discovery¹⁹. While considerable progress has been made in leveraging machine learning models for the inverse design of linear material properties (such as elastic stiffness²⁰ or Poisson's ratio²¹), extending those methods to the nonlinear regime remains challenging due to complex structure–property mappings. Recent advances have addressed this through neural network surrogates with optimization strategies^{22,23} and advanced generative models^{24,25}. However, existing inverse design methods have predominantly focused on optimizing for a single type of mechanical response at a time. A primary challenge lies in simultaneously achieving multiple

¹Mechanics and Materials Laboratory, Department of Mechanical and Process Engineering, Zürich, Switzerland. ²Department of Materials Science and Engineering, Delft University of Technology, Delft, Netherlands. ✉e-mail: sid.kumar@tudelft.nl; dmk@ethz.ch

target properties, for example, specific linear responses under small strains, while preserving desired nonlinear behaviour at large deformations. These distinct responses stem from fundamentally different deformation mechanisms that may impose conflicting requirements on the structure. The multi-objective inverse design challenge substantially increases computational complexity and intensifies the ill-posed nature of the inverse problem²⁶.

To address these challenges, diffusion models²⁷ have emerged as a promising solution for their exceptional generation quality and versatile conditioning capabilities. These models have demonstrated state-of-the-art performance across various domains, particularly in image and video synthesis²⁸, and have recently shown remarkable potential in materials design, including crystalline materials²⁹, proteins³⁰ and nonlinear metamaterials^{24,31}. By learning from existing design spaces, diffusion models capture complex underlying data distributions, enabling the efficient generation of new, coherent designs tailored to specific conditions. Despite these advances, existing works on the generative design of microstructures remain predominantly confined to two-dimensional (2D) structures with pixelated representations, limited by computational demands. While recent studies have extended to three-dimensional (3D) geometries using explicit representations such as voxels³², meshes³³ and point clouds³⁴, substantial challenges persist as explicit 3D representations are inherently data-intensive. The scarcity of high-quality training data often hinders robust learning, leading to compromised generation fidelity³² and constraining the practical applicability of generated designs.

These limitations become particularly acute for shell-based metamaterials. Characterized by thin, curved geometries, shell lattices exhibit pronounced geometric nonlinearities under large deformations, accompanied by complex phenomena including plasticity, buckling and contact. Moreover, these coupled effects are highly sensitive to geometric variations, where minor structural imperfections—such as collapsed walls, non-uniform thickness or sharp corners—can severely compromise the geometric integrity and trigger undesired behaviour. While explicit representations provide direct descriptions, precisely capturing the curvature details of shells requires extremely high-resolution discretizations, which becomes computationally prohibitive for large-scale design exploration. In contrast, implicit representations, given by simple mathematical equations, offer an efficient and robust approach for constructing shell topologies such as, for example, triply periodic minimal surfaces³⁵ and spinoid metamaterials²⁶. By tuning implicit equation parameters, one can precisely control the geometric features (for example, curvature, size, symmetry and isosurface thickness) and, consequently, tailor the mechanical properties of the resulting shell topologies, offering considerable design flexibility. Nevertheless, the relationship between implicit equations and resulting designs is a highly complex mapping: small changes in the mathematical formulation can produce vastly different topologies and properties, while very different equations may yield similar mechanical properties. This intricate mapping is a fundamental challenge for systematic design exploration. While symbolic regression is efficient in discovering interpretable analytical relationships³⁶, it is primarily suited for forward modelling and requires computationally expensive outer optimization loops for inverse design. Previous studies have primarily relied on intuitively selecting a limited set of equation templates and systematically varying numerical coefficients^{6,37}. While practical, this restricted parametric approach narrows the design space to predefined designs (for example, gyroid, primitive or diamond surfaces), potentially leading to biased, suboptimal solutions, especially when multiple target properties are involved.

To overcome these limitations, we introduce a mathematical language-based parameterization for shell metamaterials, enabling the systematic exploration of 3D implicit surfaces. Unlike existing studies that optimize parameters within fixed equation templates, our method conceptualizes implicit equations as sequences of

mathematical tokens (variables, operators, functions and constants). This equation-as-sequence paradigm systematically expands the design space beyond predefined classes, offering an efficient, flexible representation while retaining geometric characteristics of diverse shell topologies. To leverage this comprehensive design space, we propose DiffuMeta, a generative modelling framework built on diffusion transformers³⁸ (DiTs) for the inverse design of shell metamaterials with target mechanical properties. By exploiting syntactic patterns and semantic relationships in implicit equations, DiffuMeta generates diverse, physically valid shell topologies that satisfy target stress–strain responses while capturing complex physical phenomena such as buckling, plasticity and frictional contact. Our model effectively addresses the inherent ambiguity of one-to-many mappings in inverse design tasks and, distinct from previous studies targeting a single mechanical property, enables simultaneous control over multiple target properties, which may extend substantially beyond the training domain. Finally, we conduct experimental tests on 3D-printed shell structures generated by DiffuMeta to validate the model's accuracy and practical applicability.

Results

Shell metamaterial design space

We start by establishing a comprehensive design space for shell structures encompassing a broad spectrum of mechanical properties. To this end, we leverage periodic nodal surfaces³⁹, which describe smooth, continuous and non-intersecting surfaces that are periodic in all spatial dimensions. Mathematically, periodic surfaces can be represented by the nodal surface of a sum of Fourier modes⁴⁰:

$$\Psi(\mathbf{r}) = \sum_{\mathbf{k}} F(\mathbf{k}) \cos[2\pi\mathbf{k} \cdot \mathbf{r} - \alpha(\mathbf{k})] = 0, \quad (1)$$

where \mathbf{k} denotes the reciprocal vectors for a given lattice, \mathbf{r} defines a position vector in real space having Cartesian coordinates $\{x, y, z\}$, $\alpha(\mathbf{k})$ represents the phase shift and $F(\mathbf{k})$ corresponds to the amplitude associated with \mathbf{k} . For example, gyroid surfaces can be approximated by the level set of the implicit equation

$$\Psi_{\text{Gyroid}}(x, y, z) = \sin(\omega x) \cos(\omega y) + \sin(\omega y) \cos(\omega z) + \sin(\omega z) \cos(\omega x) + c = 0, \quad (2)$$

where ω defines the periodicity and the constant c determines the isovalue that controls the porosity of the generated surface. Such representations based on trigonometric functions provide a compact yet highly adaptable framework for generating diverse periodic shell topologies. To systematically expand the design space, we construct a library of Fourier-type basis functions $T_j(x, y, z)$ (Supplementary Table 1), including trigonometric functions (for example, $\sin(x)$, $\cos(y)$) and their low-order multiplicative combinations (for example, $\sin(x)\cos(y)$). Using this library, we assemble implicit surface equations by strategically combining those terms with randomly sampled coefficients. The general form of our candidate implicit equations can be represented as

$$\Psi(x, y, z) = \sum_{j \in \mathcal{J}} \alpha_j T_j(x, y, z) + c = 0, \quad \text{with } \mathcal{J} \subset \{1, 2, \dots, N\}, \quad (3)$$

$$1 \leq |\mathcal{J}| \leq 3,$$

where N is the total number of tokens in that library, α_j are their corresponding coefficients and c is a constant offset. Despite the apparent simplicity of the base library, the combinatorial construction provides a vast design space of up to $\sim 10^{12}$ possible expressions (Supplementary Section 1.2). Furthermore, our approach is inherently generalizable and readily adaptable to broader function sets, such as exponential functions, logarithmic functions, polynomial terms, enabling extension to a wider range of functional forms. To ensure physical feasibility, we

verify that the generated surfaces are self-connected and periodic in all spatial dimensions, and disregard disjoint surfaces (Supplementary Section 1). The coefficients α_i and constant offset c are drawn from a uniformly spaced grid spanning $(-6, 6)$ in increments of 0.1, providing extensive parameter coverage while ensuring computational tractability (see also Supplementary Table 2 for a systematic evaluation of different sampling schemes).

To efficiently represent this diverse design space, we develop an algebraic language-based parameterization that decomposes each equation into a sequence of discrete mathematical tokens of three types: trigonometric function groups (for example, $\sin(x)\cos(y)$), numeric coefficients and arithmetic operators (for example, $+$, $-$). These components define a mathematical vocabulary that enables systematic generation and analysis of implicit surfaces within a unified language-modelling framework (Fig. 1a). Any given implicit equation $\Psi(x, y, z)$ can hence be represented as a sequence $w = [w_0, w_1, \dots, w_n]$ of length n , each w_i corresponding to the i th token. For example, the gyroid surface equation in equation (2) for $\omega = 1$ can be tokenized as

$$w = [+ , 1 , . , 0 , \sin(y) \cos(z) , + , 1 , . , 0 , \sin(x) \cos(y) , + , 1 , . , 0 , \sin(z) \cos(x) , [\text{PAD}] , \dots] \quad (4)$$

Each sequence is padded to the maximum sequence length L to ensure uniform dimensionality across the dataset. This equation-as-sequence strategy provides a compact yet precise representation that preserves the mathematical integrity of implicit surfaces, with markedly reduced dimensionality compared with explicit representations. By conceptualizing implicit equations as a mathematical language, our approach captures contextual dependencies among equation components, enabling the application of natural language processing techniques to generate new shell metamaterial designs.

By systematically varying the basis functions and coefficients, we construct a rich database containing 23,534 unique shell topologies, ensuring broad coverage of the design space with diverse mechanical behaviours (Supplementary Section 1). The wall thickness of each unit cell is scaled to maintain a constant relative density (fill fraction) of $\rho = 0.1$. To characterize their mechanical behaviour, we evaluate the stress-strain responses of each design via FE analysis (Fig. 1b). The shell unit cell ($10 \text{ mm} \times 10 \text{ mm} \times 10 \text{ mm}$) is positioned between two rigid plates with periodic boundary conditions along all lateral directions. Shell structures are modelled as an elastoplastic material calibrated to an in-house 3D-printing elastomer⁴¹, accounting for frictional contact. We apply quasi-static compressive strain up to $\varepsilon = 30\%$ through the upper plate in the \hat{e}_3 -direction, emulating loading scenarios for footwear cushioning⁴² and impact absorption⁴³. In addition, we compute the effective stiffness tensor through FE homogenization of a single unit cell with periodic boundary conditions. For each shell structure represented by its implicit equation Ψ , we collect its compressive stress response $\sigma \in \mathbb{R}^{11}$ evaluated at 11 selected strain levels (Methods and Supplementary Section 2), as well as the corresponding homogenized stiffness tensor $\mathbb{C} \in \mathbb{R}^{6 \times 6}$. This defines our dataset $\mathcal{D} = \{(\Psi^{(n)}, \sigma^{(n)}, \mathbb{C}^{(n)}) : n = 1, \dots, N\}$, comprising N structure-response pairs. This yields a versatile library of periodic shell surfaces, encompassing both classical minimal surface geometries (for example, Schwarz P and D, and gyroids) and not frequently studied morphologies, altogether exhibiting diverse stress-strain responses (Fig. 1c).

Diffusion-based generative modelling framework

The proposed language-based parameterization provides a compact, efficient representation for diverse shell topologies. A fundamental challenge lies in the complex, many-to-many mapping between algebraic sequences and resulting shell topologies. This relationship is highly nonlinear, with seemingly distinct mathematical formulations producing similar geometries, while minor variations in coefficients may lead to drastically different topologies (Supplementary Fig. 1).

Such ambiguity, coupled with the high-dimensional parameter space, creates an intricate design landscape that renders traditional optimization approaches ineffective: motivating our use of a diffusion-based framework that learns complex structure-property relationships directly from data.

Diffusion models²⁷ are probabilistic generative models that learn to reverse a gradual noising process, enabling the generation of high-quality samples from complex data distributions. While they excel in continuous domains such as computer vision (using U-Net architectures⁴⁴), their application to discrete textual data remains challenging due to the gap between continuous diffusion processes and discrete inputs⁴⁵. To this end, we adopt the Diffusion-LM architecture⁴⁵ and apply an embedding function $e_\phi(\cdot)$, which maps each token onto a continuous vector in \mathbb{R}^d . Given a shell geometry, its corresponding implicit equation is tokenized as a sequence $w = [w_1, w_2, \dots, w_n]$. The i th token w_i may correspond to a function, operator or constant. Each token then undergoes an embedding to yield the embedding of the sequence as

$$e_\phi(w) = [e_\phi(w_1), e_\phi(w_2), \dots, e_\phi(w_n)]^T \in \mathbb{R}^{n \times d}, \quad (5)$$

where d is a hyperparameter denoting the embedding dimension. The reverse process aims to recover the original input embeddings through iterative denoising, which are subsequently mapped back to the discrete sequence w via a trainable rounding step (applying a softmax function at each position and selecting the most likely token). In this work, we jointly train the diffusion model and embedding function end-to-end, which allows the embedding space to evolve alongside the diffusion process to improve generation quality.

As shown in Fig. 2, our DiffuMeta framework formulates the inverse design of shell metamaterials as a conditional denoising diffusion process. The forward process progressively adds Gaussian noise to the embeddings over T timesteps. During reverse denoising, the DiT iteratively removes this noise from randomly sampled noisy embeddings to reconstruct physically meaningful implicit equations. To guide the generation towards desired properties, we use classifier-free guidance⁴⁶, which directly incorporates conditioning labels \mathbf{c} without requiring auxiliary classifiers (Methods). As the backbone denoising network, we adopt a transformer architecture adapted from DiTs³⁸ to learn the reverse process. The transformer's ability to capture sequential dependencies is particularly well-suited for modelling implicit equations, where small perturbations can substantially affect the resulting shell geometry and its properties. The target properties, including the stress responses σ and the homogenized elastic properties (for example, effective Poisson's ratios), are projected to high-dimensional embeddings by (learnable) linear layers, which are then integrated into the DiT model via cross-attention mechanisms⁴⁷ and adaptive layer norm³⁸ (adaLN) blocks as conditioning labels (Supplementary Sections 3 and 4).

Guided design of shell metamaterials

We first demonstrate that our DiffuMeta framework successfully captures the underlying data distribution and generates unseen, physically realizable shell structures. We generate 200 implicit equations in an unconditional setting and evaluate the generation quality using three key metrics: (1) validity, the percentage of valid implicit equations producing single-connected surfaces without disjoint components; (2) novelty, the percentage of valid shell geometries not found in the training dataset and (3) uniqueness, the percentage of unique shell structures among the valid shells. Our model achieves an overall validity of 74.0%, a novelty score of 100% and a uniqueness score of 100%. Notably, this validity rate far exceeds the 3.2% validity rate achieved by random sampling of implicit equations within the design space (Supplementary Section 6.2), highlighting the model's ability to avoid trivial solutions while effectively generating diverse, physically

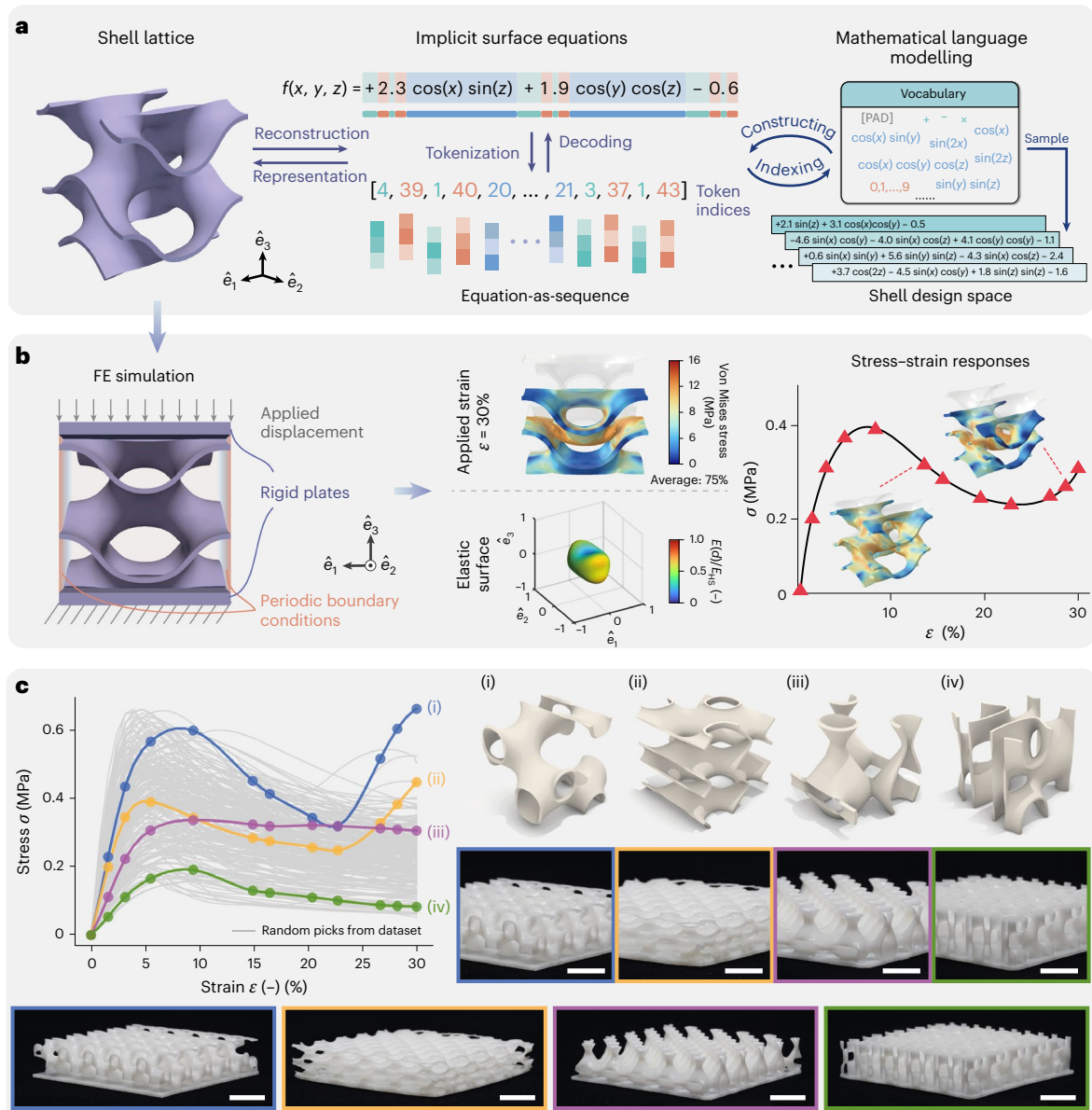


Fig. 1 | Overview of the shell-based metamaterial parameterization and design space generation process. a, A shell lattice is generated from the implicit level set equation, which can be tokenized into a sequence of discrete mathematical tokens drawn from a structured vocabulary. New shell designs can be generated by sampling and recombining these tokens. **b**, To obtain the stress-strain responses, we conduct FE simulations by imposing rigid plates on the top and the bottom with periodic boundary conditions on the lateral surfaces. A quasi-static compressive strain of up to 30% along the \hat{e}_3 -direction is applied. The overall effective stress-strain response is extracted from the

reaction forces. A representative deformed shell unit cell is shown at an applied strain of 30%. Also shown is the 3D elastic surface plot illustrating the directional effective Young's modulus (obtained via FE homogenization). **c**, Stress-strain responses of 200 structures randomly drawn from the dataset, and selected representative examples with distinct mechanical behaviours. Also shown are the photos of fabricated shell structures, each obtained by arranging corresponding shell unit cells in a $5 \times 5 \times 1$ array, with a total size of $50 \text{ mm} \times 50 \text{ mm} \times 10 \text{ mm}$. Scale bars: 10 mm.

meaningful structures. The generated designs exhibit diverse mechanical behaviours and distinct new topologies (Supplementary Fig. 8), enabling efficient generation of diverse valid designs at negligible computational cost. We emphasize that the mapping from discrete implicit equations to continuous surface geometries is inherently challenging: no existing method directly evaluates the quality of resulting surface geometries from symbolic equations alone. The high validity and uniqueness scores confirm the model's ability to capture the complex shell design space, while the high novelty rate underscores its ability to extrapolate beyond the training data.

Next, we evaluate DiffuMeta's performance in the guided generation of shell designs that match target nonlinear stress-strain

responses. As a first example (Fig. 3a), we select a target response with pronounced softening after reaching a peak stress. The designs proposed by DiffuMeta closely match the target response, achieving normalized root mean squared error (n.r.m.s.e.; e) values of the FE-calculated response versus target response ranging from 3.3% to 3.6% (compared with 5.0% for the closest existing design in the training dataset). Second, we consider a target response with notable softening at -8% applied strain, followed by hardening and a gradual stress increase as the structure compresses further (above 25%; Fig. 3b). While the best match in the training dataset achieves an n.r.m.s.e. of $e = 7.7\%$, our inverse-designed solutions show improved performance, with the best achieving 4.6% and variations ranging up to 8.5%. The generated

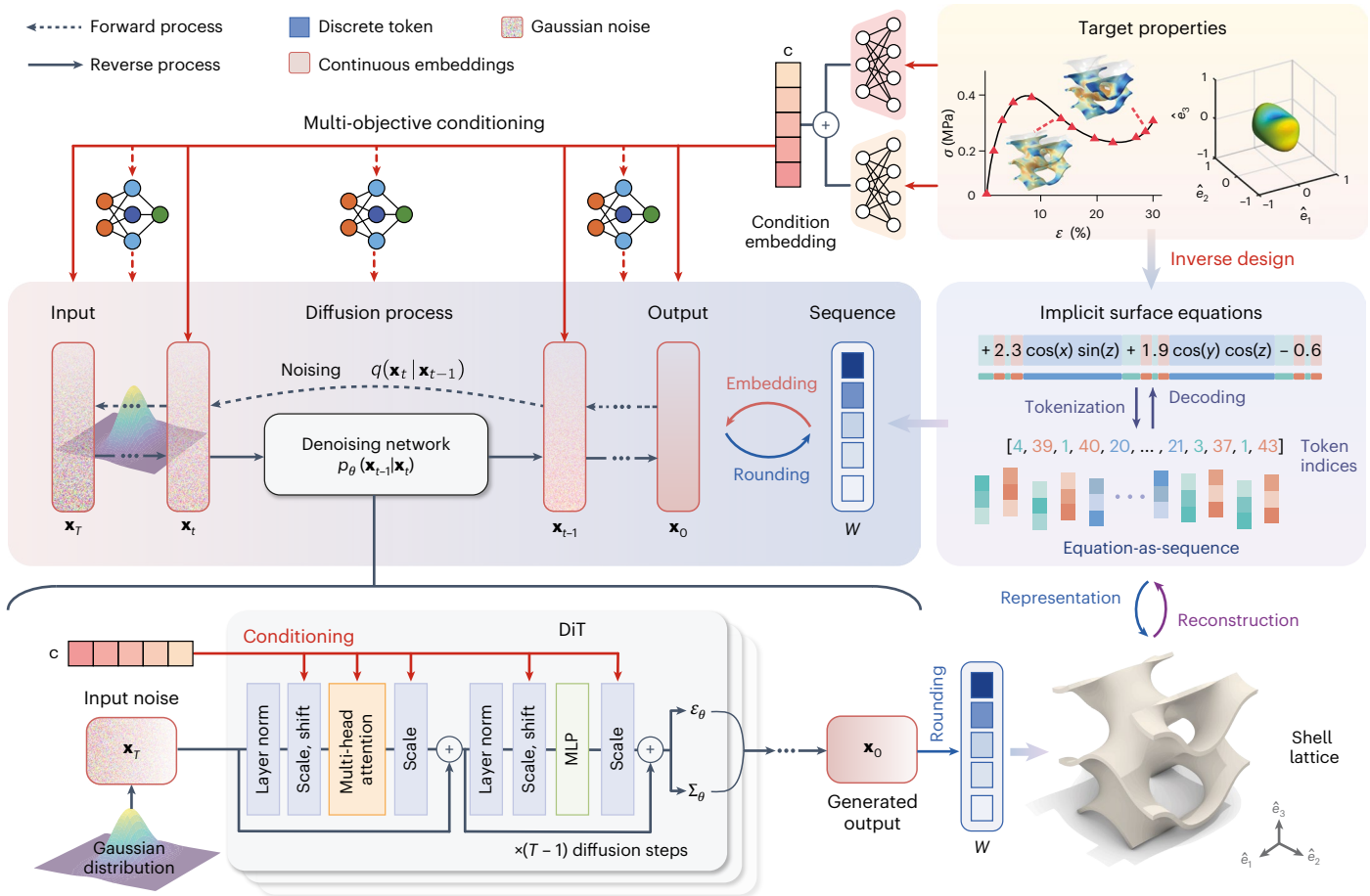


Fig. 2 | Schematic overview of the DiffuMeta framework for the inverse design of shell metamaterials with target mechanical properties. The process begins with discrete equation sequences representing implicit surface geometries, which are converted into a continuous space. During the forward (noising) process, Gaussian noise is progressively added to the embeddings over T timesteps. The reverse (denoising) process uses a DiT to iteratively remove noise and reconstruct the original embeddings. To enable property-conditioned

generation, target mechanical properties (stress–strain responses σ and homogenized stiffness tensor C) are encoded into conditioning embeddings and integrated into the denoising network through cross-attention and adaLN mechanisms. Following denoising, a trainable rounding step maps the continuous outputs back to discrete token sequences, which are then decoded to generate the corresponding shell geometries with desired mechanical characteristics. MLP, multilayer perceptron.

shell structures successfully capture the characteristic stress increase at higher strains by leveraging contact interactions between structural elements, demonstrating the model's ability to predict complex deformation mechanisms under large deformations. Compared with direct dataset search, our method generates diverse new designs not present in the training data while achieving the same target properties and, more importantly, at negligible computational cost (~ 0.22 seconds per design on a single graphical processing unit; Supplementary Section 5). Notably, the generated structures in Fig. 3a(i),b(i) have nearly identical geometries, differing only in minor variations of local pore morphology and curvature, yet they produce substantially different mechanical responses. The corresponding implicit equations for generated shell designs are provided in Supplementary Section 6.3, revealing that their geometric similarity cannot be inferred from their drastically different mathematical formulations. This contrast underscores the critical challenge in the inverse design of nonlinear metamaterials, where subtle geometric variations can lead to substantial changes in mechanical behaviour due to the complex structural interactions, while DiffuMeta efficiently captures this intricate structure-to-property mapping.

A further key advantage of DiffuMeta lies in its ability to generate multiple distinct designs for the same target response, addressing the fundamental one-to-many mapping challenge in inverse design problems (that is, multiple designs can produce similar mechanical behaviour). The overall performance distributions show that the model

consistently generates multiple designs whose properties closely match the target responses (Supplementary Fig. 6), demonstrating stable and robust inverse design performance. Unlike traditional optimization methods such as topology optimization, which typically converge to a single solution⁴⁸, our generative approach naturally produces diverse candidates that all satisfy the specified targets. Notably, the generated structures exhibit diverse geometries (for example, variations in surface curvature, pore distribution patterns and local feature dimensions), while they consistently reproduce key mechanical properties, such as initial stiffness, softening, plateau stress and hardening, through distinct deformation mechanisms, as evidenced by the von Mises stress distribution plots. In addition, the elastic surface plots of generated designs in Fig. 3a,b reveal that each design exhibits unique anisotropic elastic properties, offering potential design flexibility for applications requiring secondary performance criteria.

Inverse design of shell metamaterials for unseen target properties

So far, we have demonstrated DiffuMeta's capability to generate new shell designs conditioned on complex stress–strain responses. While the target responses in Fig. 3 lie within the training distribution and can be reasonably matched by existing designs, we next assess the model's extrapolation ability by examining two target stress–strain curves that exhibit highly nonlinear, non-monotonic compressive responses,

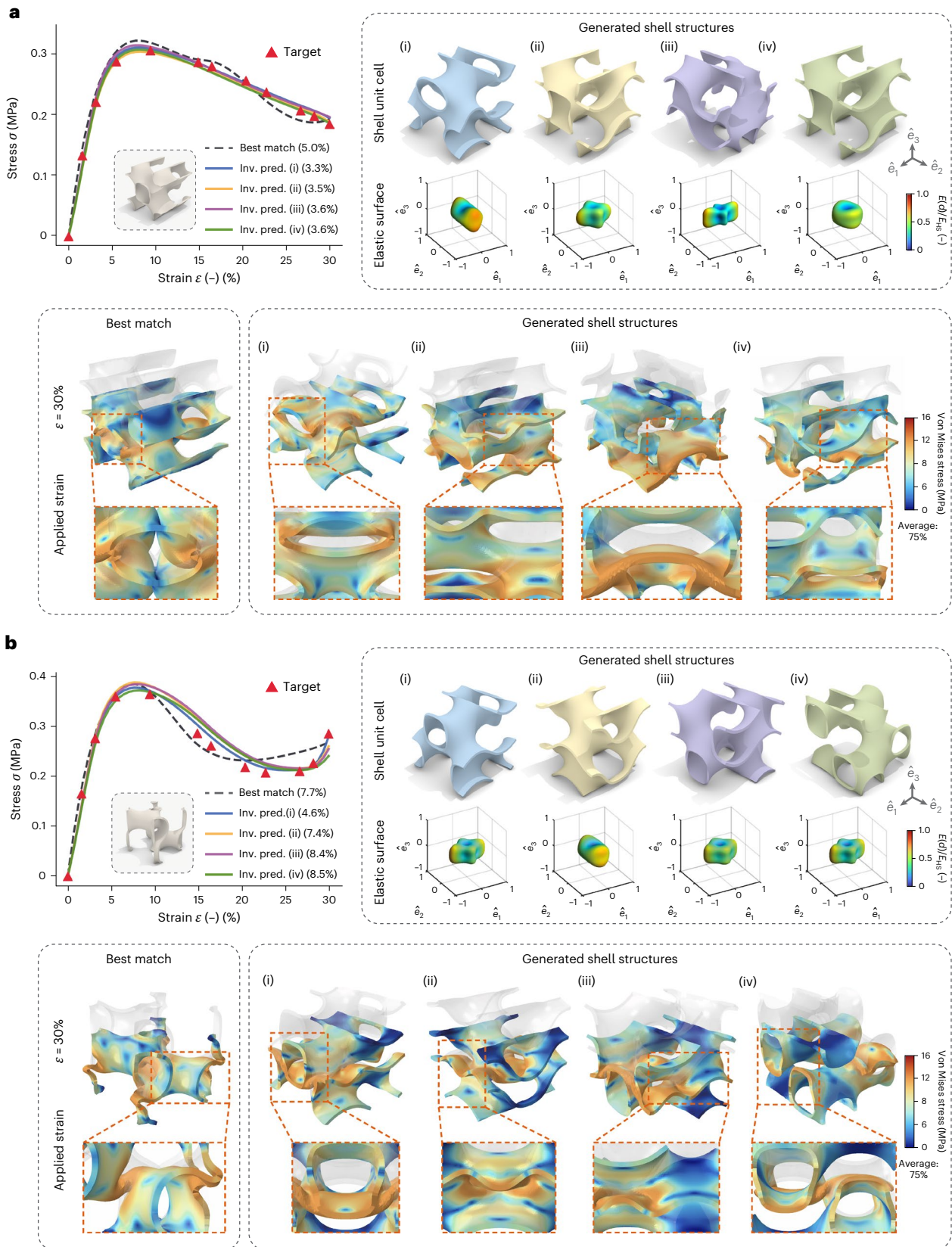


Fig. 3 | Inverse design of shell metamaterials with target compressive stress-strain responses. a, b. The model is conditioned on target responses (denoted by red triangles) exhibiting pronounced softening (a) and initial softening and subsequent hardening (b). Generated designs (i)–(iv) show diverse geometric configurations that achieve similar mechanical behaviour through different deformation mechanisms. Each example shows the deformed unit cells of both the best match from the training dataset and the generated designs at 30% strain,

revealing varying stress distributions and structural responses. Elastic surface plots demonstrate distinct anisotropic 3D elastic stiffnesses for each generated design (normalized by the isotropic Hashin and Shtrikman (HS) upper bounds, E_{HS}). All shown stress–strain responses and elastic surfaces were obtained via FE analysis, with n.r.m.s.e. values (in brackets) quantifying design accuracy relative to target responses. inv. pred., inverse prediction.

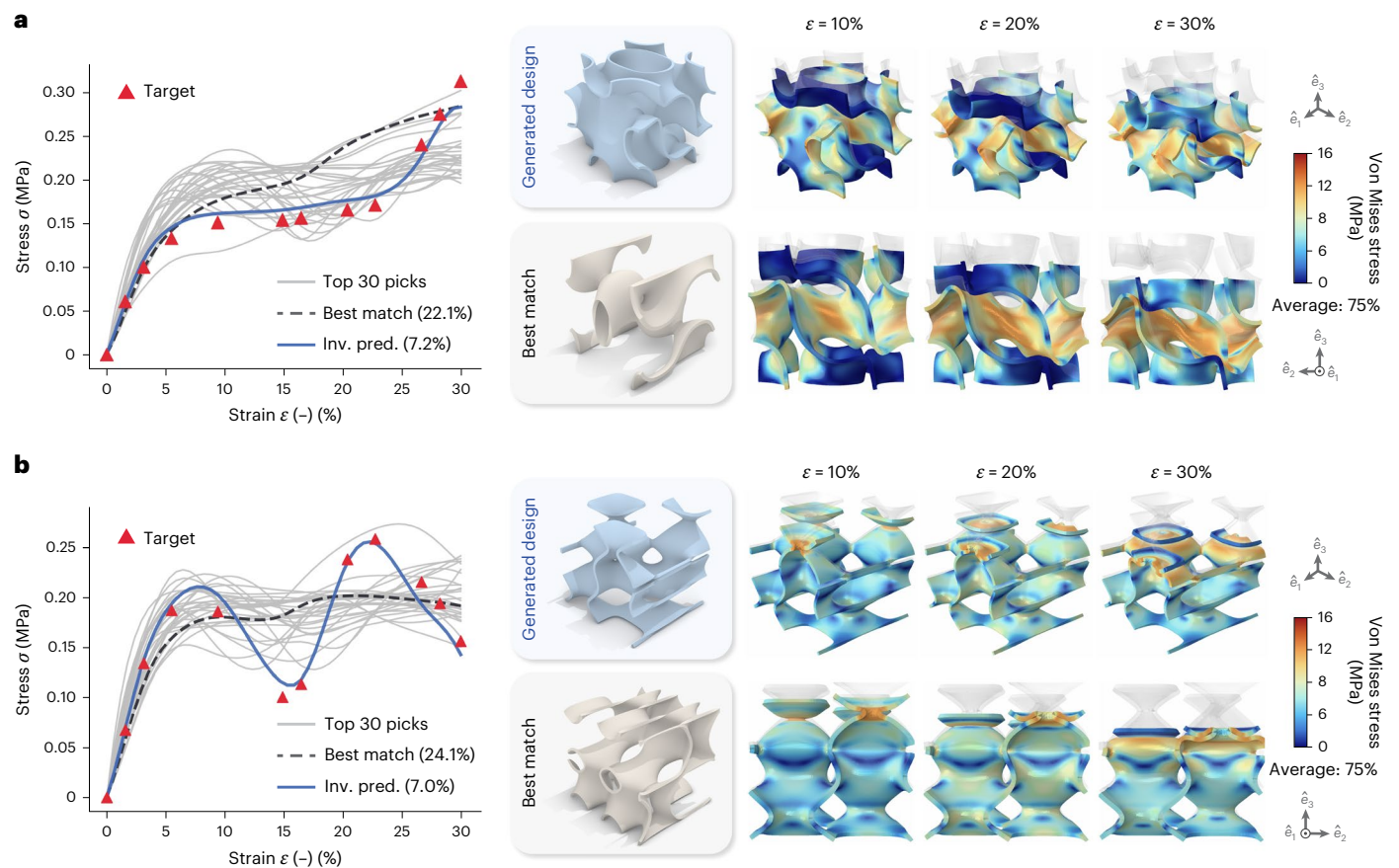


Fig. 4 | Inverse-designed shell metamaterials with unseen stress–strain responses. a, b. The diffusion model generates designs conditioned on target stress–strain curves (denoted by red triangles) exhibiting a stress plateau and subsequent hardening (a) and pronounced buckling-induced stress peaks at 8% and 22% strain (b). These responses extend well beyond the training distribution.

We highlight the top 30 closest matches from the training set in grey in a and b, selected based on n.r.m.s.e., which deviate substantially from the target. All shown stress–strain responses and elastic surfaces were obtained via FE analysis, with n.r.m.s.e. values (in brackets) quantifying design accuracy relative to target responses.

deviating substantially from the training distribution. The target curve in Fig. 4a shows a stress plateau followed by strain hardening. The second target response (Fig. 4b) exhibits two pronounced stress peaks. In both cases, the best matches from the training dataset poorly reconstruct the target response ($e = 22.1\%$ and $e = 24.1\%$, respectively), which is unsurprising, indicating the vastness of the design space (and the small training set). We also show the top 30 candidate designs from the training dataset, which generally deviate from the target, particularly at large strains. In contrast, the model identifies designs that accurately reproduce the complex target responses (achieving $e = 7.2\%$ and $e = 7.0\%$, respectively).

As shown in Fig. 4a, the generated structure initially undergoes progressive shell bending, followed by contact between opposing surfaces, which creates new internal load paths and stiffens the structure, producing the characteristic stress rise at large strains. In contrast, the design in Fig. 4b exhibits a sequential deformation mechanism characterized by initial elastic buckling of its curved surfaces ($\epsilon < 15\%$), which causes softening, followed by the development of multiple contact interfaces, which leads to hardening, and finally another local buckling instability that results in the second softening phase at around 22% applied strain. These highly nonlinear stress–strain responses of shell lattices at finite strains emerge from intricate structural interactions rather than being explicitly encoded in their implicit equations. The mapping from abstract mathematical representations, which define only the initial topology, to these sophisticated nonlinear responses is therefore challenging. Nevertheless, DiffuMeta successfully learns this intricate relationship by identifying mathematical patterns that

correlate geometric features with the resulting deformation characteristics of various shell metamaterials.

Multi-target conditional generation of shell metamaterials

To demonstrate our framework's ability to extend beyond a single design objective, we condition the generation of shell metamaterials on multiple target properties simultaneously (Methods). We focus on the task of jointly tuning both linear and nonlinear mechanical responses, for example, the effective (anisotropic) Poisson's ratio and the nonlinear compressive stress–strain response. Such design targets can be leveraged for applications in, for example, protective gear or biomedical implants, where a specific nonlinear stress–strain response (such as controlled buckling or energy absorption) is required, while also ensuring, for example, auxetic behaviour under small-strain compression to enhance conformability and mechanical stability.

As a first example, we consider a target stress–strain response exhibiting pronounced softening under compression, while simultaneously targeting three distinct effective Poisson's ratios (measured at small strains): $\nu_{32} = -3.0$ (strongly auxetic), $\nu_{32} = 0$ (zero transverse strain) and $\nu_{32} = 1.0$ (high positive Poisson's ratio). As shown in Fig. 5a, the generated shell structures not only closely reproduce the target stress–strain responses (ranging from $e = 4.7\%$ to $e = 10.4\%$) but also exhibit the intended Poisson effect. Figure 5a further compares the homogenized response of the closest design in the training set ($e = 11.2\%$) with their deformed states at 10% compressive strain under periodic boundary conditions. In contrast to the best match, which exhibits moderate lateral expansion, the generated designs demonstrate

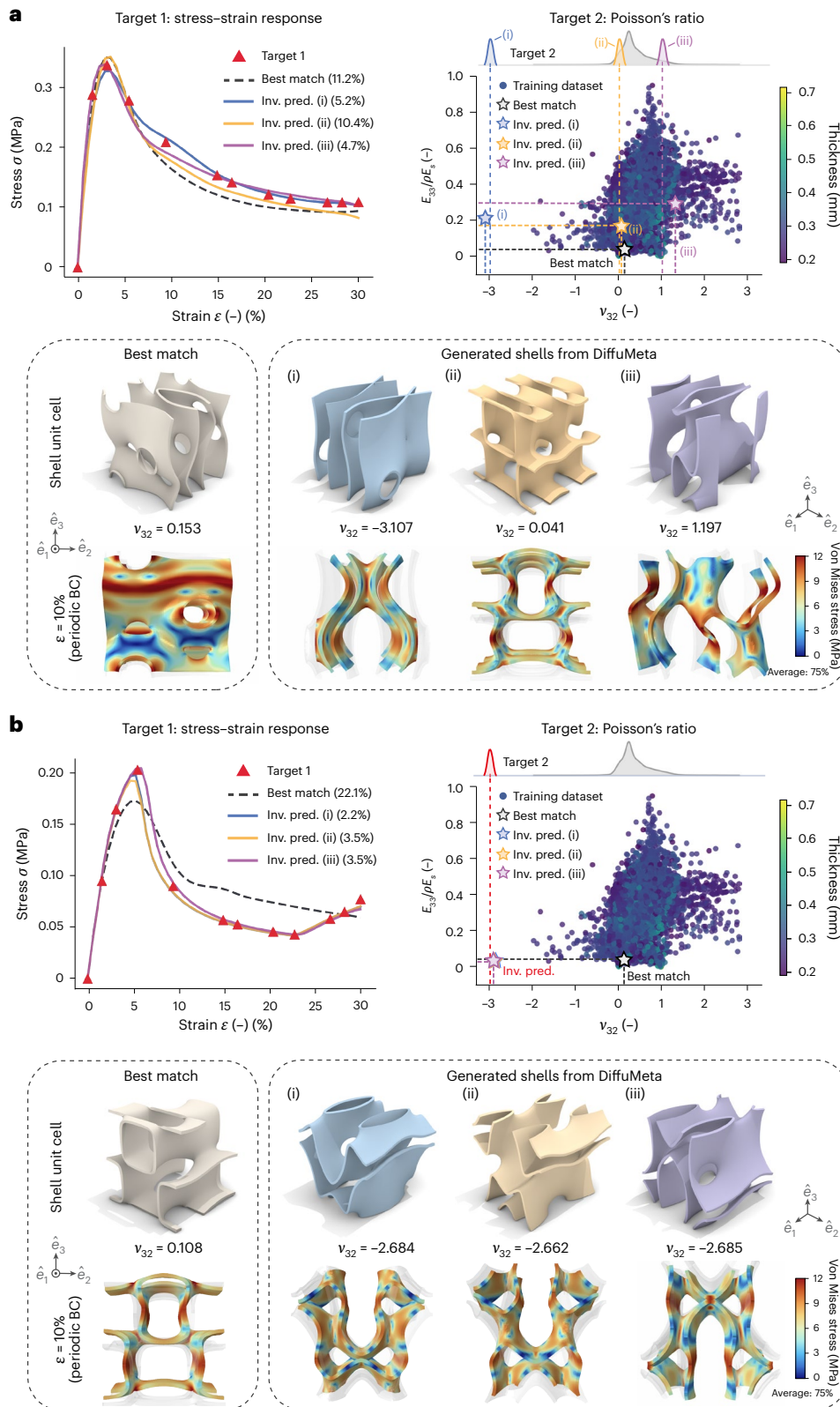


Fig. 5 | Multi-target conditional generation of shell metamaterials.

a, Generated shell designs conditioned on a target stress–strain response while achieving three distinct target effective (anisotropic) Poisson's ratios (measured at small strains): $\nu_{32} = -3.0$, $\nu_{32} = 0$ and $\nu_{32} = 1.0$. **b**, Inverse design for unseen target property combinations, where both the stress–strain response and Poisson's ratio ($\nu_{32} = -3.0$) extend well beyond the training distribution. Each example shows the achieved Poisson's ratio of the best match from the training dataset and the generated designs, compared with the distribution of training samples

in the relevant property space (each dot represents a unit cell in the training data, colour-coded by shell thickness). The effective directional Young's modulus E_{33} is normalized by the Young's modulus of the base material E_s and the relative density ρ . The simulated samples at 10% compressive strain illustrate their lateral deformations. All shown stress–strain responses were obtained via FE analysis, with n.r.m.s.e. values (in brackets) quantifying design accuracy relative to target responses.

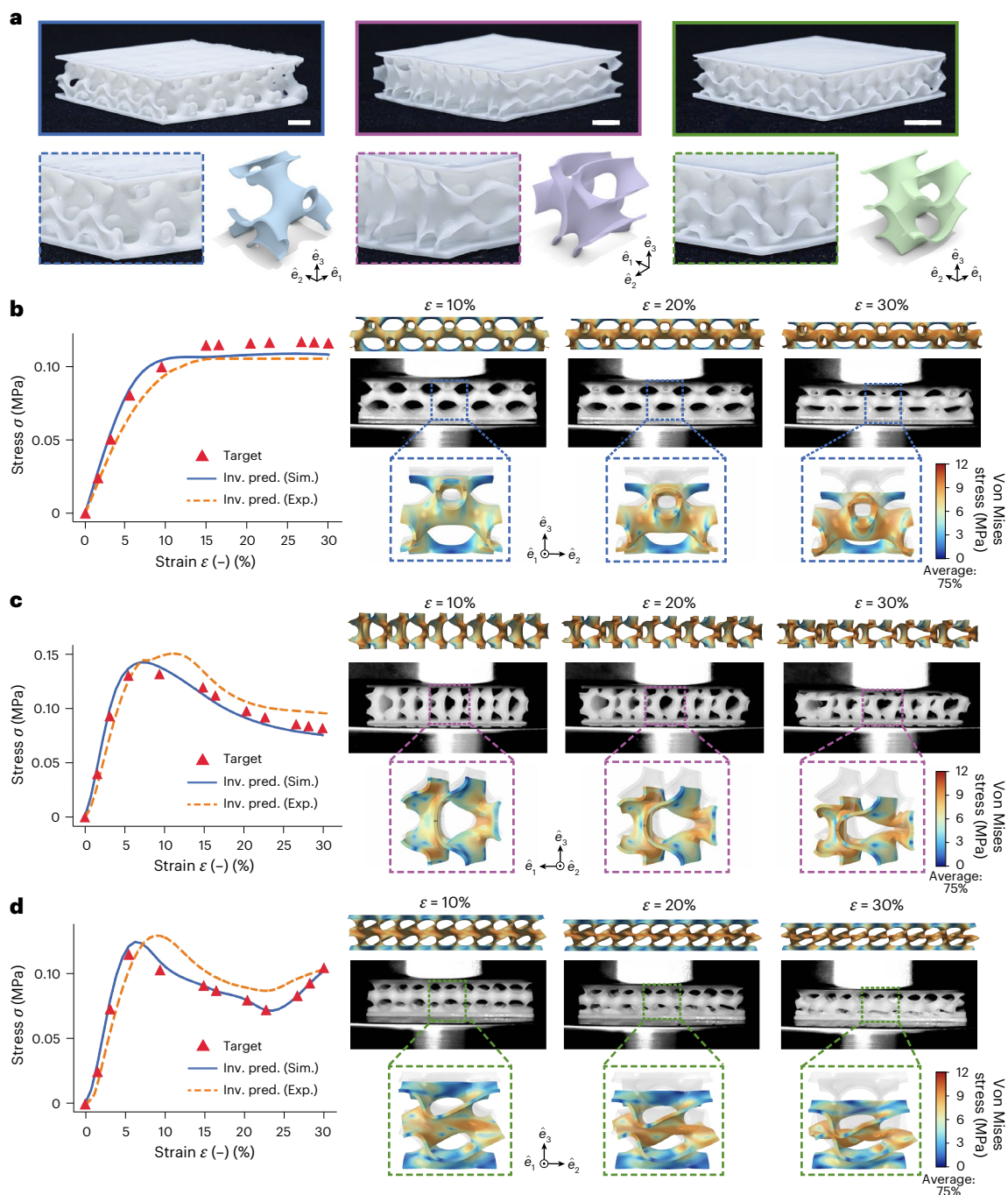


Fig. 6 | Experimental validation of shell metamaterials generated by DiffuMeta. a, Fabricated representative shell samples alongside their corresponding computer-aided design models. Samples are arranged in $5 \times 5 \times 1$ arrays with 10% relative density. Scale bars: 10 mm. **b–d**, Comparison between experimental (Exp.) stress–strain responses (dashed lines) and FE simulation (Sim.) results (solid lines) for three distinct shell designs generated by DiffuMeta, exhibiting an extended stress plateau (**b**), pronounced softening (**c**) and initial

softening followed by hardening (**d**), respectively. Target responses used as conditions for the diffusion model are indicated with red triangles. The deformed configurations of generated shell unit cells obtained from FE analysis at different strain levels are shown in $5 \times 5 \times 1$ tessellations for visualization. The experimental results demonstrate overall good agreement with both the target responses and simulation predictions for the nonlinear behaviour, validating the effectiveness of the inverse design framework. Scale bars, 10 mm.

diverse lateral deformation behaviours. The auxetic design Fig. 5a(i) undergoes substantial lateral contraction on compression, achieving the target negative Poisson's ratio through inward bending of its curved surfaces. Design Fig. 5a(ii) shows pronounced lateral expansion, while design Fig. 5a(iii) maintains nearly constant lateral dimensions. The corresponding von Mises stress distribution plots further reveal that each geometry accommodates the applied compressive load through distinct deformation pathways and stress localization

patterns to maintain the same target stress–strain responses while achieving various Poisson's ratios targets. (It is remarkable that the linear Poisson's ratio, a measure valid at small strains, here serves well as an effective descriptor also for the nonlinear, large-strain lateral sample deformation.)

As a second example, we consider a target stress–strain response with pronounced softening followed by stiffness increase at higher strains (Fig. 5b), which lies outside the training distribution, as

evidenced by the poor match ($e = 22.1\%$) with the best training dataset candidate. Despite this challenging unseen target, the inverse-designed solutions closely follow the target curve and achieve substantially lower errors (2.2–3.5%). In addition, the inverse-designed solutions successfully produce the desired extreme auxetic behaviour, exhibiting pronounced lateral contraction under compression. Notably, the target Poisson's ratio of $\nu_{32} = -3.0$ also lies far outside the training distribution, as evidenced by the scatter plot of effective modulus versus Poisson's ratio for all training samples. Importantly, the generated designs achieving exceptional properties (Figs. 4 and 5) remain strictly within the defined design space bounds, with all coefficient values within the training range (Supplementary Section 6.3). This demonstrates that DiffuMeta achieves extrapolation in the property space through interpolation in the design space by capturing the complex underlying structure–property relationships governing highly nonlinear behaviours, including plasticity, buckling, contact and so on. Collectively, these results demonstrate the robust generalization capability of the proposed framework, enabling the inverse design of shell metamaterials with highly non-trivial combinations of unseen linear and nonlinear mechanical properties, surpassing the limits of the training distribution.

Experimental validation

To validate our inverse design framework, we conduct experimental compression tests on 3D-printed shell samples generated by DiffuMeta (Methods). We select several distinct target responses from the test dataset (unseen during training) and fabricate the corresponding generated designs (Fig. 6a). Figure 6b–d presents uniaxial compression test data in comparison with FE results. The experimental validation demonstrates overall good agreement between simulated and measured stress–strain responses, validating both the FE modelling accuracy and the robustness of our inverse design framework. The design in Fig. 6b shows an extended stress plateau up to high strains, maintaining structural integrity through its smooth, continuous surfaces without notable buckling instabilities. In contrast, Fig. 6c demonstrates pronounced softening, characterized by localized surface buckling. Figure 6d illustrates a more complex target response featuring initial softening followed by hardening, which results from progressive contact formation between internal surfaces under large deformations. Notably, the fabricated samples successfully reproduce the complex nonlinear mechanical behaviours predicted by DiffuMeta, including a stable plateau, buckling-induced softening and hardening due to contact. While some discrepancies exist between simulation and experiment due to, for example, material variations, geometric imperfections and fabrication-induced residual stresses, the overall stress–strain responses and key mechanical features are well captured experimentally. This close agreement validates the robustness and practical applicability of our inverse design framework, opening new possibilities for creating new materials with tailored nonlinear responses for applications in soft robotics, morphing structures and energy-absorbing systems.

Discussion

The presented generative modelling framework enables the inverse design of architected materials with precisely targeted combinations of nonlinear stress–strain responses and linear elastic properties, demonstrating robust extrapolation beyond the training domain. DiffuMeta uses a new algebraic language-based parameterization that represents implicit equations as discrete token sequences. This provides a flexible, low-dimensional representation encoding a vast shell design space, while preserving intricate topological features essential for their mechanical functionality. By integrating these sequences into a diffusion-based framework, DiffuMeta effectively learns how subtle variations in implicit equations lead to substantial changes in mechanical performance, capturing the complex mappings between abstract implicit equations and highly non-trivial deformation mechanics, including buckling and contact.

A key advantage of our approach lies in the probabilistic nature of the diffusion model, which inherently addresses the ill-posedness of the inverse design problem by generating multiple solutions for a given target response, unlike conventional optimization methods that converge to a single solution and depend heavily on initialization. In addition, the framework demonstrates strong generalization, successfully identifying designs for highly non-trivial unseen target responses. Furthermore, our approach enables multi-objective conditional generation, simultaneously controlling linear and nonlinear properties while effectively addressing the complex coupling between different mechanical responses.

We note that our framework requires target properties to be physically achievable within the shell metamaterial design space. While the model successfully generates designs that extend beyond existing property boundaries (Figs. 4 and 5), this extrapolation capability is inherently bounded by the physics encoded in the training data; targets requiring mechanical mechanisms not represented in the dataset would necessitate expanding the training data to include richer mechanical responses (for example, hierarchical designs, multi-stage plasticity or snap-through instabilities). Furthermore, the current approach does not explicitly incorporate physical constraints during generation, which may occasionally yield designs that, while mathematically valid, are challenging to fabricate. Future work could integrate physics-informed constraints directly into the diffusion process⁴⁹ to enhance robustness and physical validity. In addition, active learning strategies⁵⁰ could be used to iteratively sample underrepresented regions of the design space, improving generation quality for out-of-distribution targets. The versatility and efficiency of DiffuMeta make it readily available for extension to other metamaterial architectures⁵¹ and targeting alternative properties, such as impact absorption^{23,43}, optical responses⁵² and multiphysics properties⁵³, by altering the training dataset accordingly. The framework could also be integrated with large language models to enable natural language-driven design specifications⁵⁴, further enhancing the design of multifunctional metamaterials. These extensions underscore the potential of our generative modelling approach, offering a scalable and generalizable framework for the inverse design of diverse metamaterial systems with unprecedented capabilities.

Methods

We here provide details of the diffusion model derivation and architecture, the FE simulation setup to evaluate the stress–strain response of shell lattices, and fabrication and experimental characterization details. Further explanations can be found in the Supplementary Information.

Denosing diffusion models

At its core, a diffusion model consists of two fundamental processes: forward and reverse. The forward process systematically perturbs the input data $\mathbf{x}_0 - q(\mathbf{x})$ by gradually adding Gaussian noise over T steps, transforming it into a standard Gaussian noise $\mathbf{x}_T \sim \mathcal{N}(0, \mathbf{I})$. This noise injection follows a fixed Markov chain, in which each transition from \mathbf{x}_{t-1} to \mathbf{x}_t is governed by

$$q(\mathbf{x}_t | \mathbf{x}_{t-1}) = \mathcal{N}(\mathbf{x}_t; \sqrt{1 - \beta_t} \mathbf{x}_{t-1}, \beta_t \mathbf{I}), \quad (6)$$

where the hyperparameter $\{\beta_t \in (0, 1)\}_{t=1}^T$ regulates the amount of noise added at diffusion step t . We can then sample \mathbf{x}_t at any time step t during the forward process by

$$q(\mathbf{x}_t | \mathbf{x}_0) = \mathcal{N}(\mathbf{x}_t; \sqrt{\bar{\alpha}_t} \mathbf{x}_0, (1 - \bar{\alpha}_t) \mathbf{I}), \quad \text{where } \alpha_t = 1 - \beta_t, \bar{\alpha}_t = \prod_{i=1}^t \alpha_i \quad (7)$$

$$\mathbf{x}_t = \sqrt{\bar{\alpha}_t} \mathbf{x}_0 + \sqrt{1 - \bar{\alpha}_t} \boldsymbol{\varepsilon}, \quad \boldsymbol{\varepsilon} \sim \mathcal{N}(0, \mathbf{I}).$$

The reverse denoising process seeks to reconstruct the original data \mathbf{x}_0 by first sampling from $q(\mathbf{x}_t)$ and then proceeding in reverse time

direction, sampling from $q(\mathbf{x}_{t-1}|\mathbf{x}_t)$ until \mathbf{x}_0 . Since the true denoising transition $q(\mathbf{x}_{t-1}|\mathbf{x}_t, \mathbf{x}_0)$ is intractable, we can approximate it using a neural network $p_\theta(\mathbf{x}_{t-1}|\mathbf{x}_t)$ parameterized by θ . The reverse process $p_\theta(\mathbf{x}_{0:T})$ is characterized as a Markov chain as

$$p_\theta(\mathbf{x}_{0:T}) = p(\mathbf{x}_T) \prod_{t=1}^T p_\theta(\mathbf{x}_{t-1}|\mathbf{x}_t), p_\theta(\mathbf{x}_{t-1}|\mathbf{x}_t) = \mathcal{N}(\mathbf{x}_{t-1}; \mu_\theta(\mathbf{x}_t, t), \sigma_t^2), \quad (8)$$

where $p(\mathbf{x}_T) = \mathcal{N}(\mathbf{x}_T; 0, I)$ denotes the standard Gaussian distribution, $\mu_\theta(\cdot)$ is the predicted mean of the Gaussian transition $q(\mathbf{x}_{t-1}|\mathbf{x}_t)$, and σ_t^2 is a variance depending on the time step: $\sigma_t^2 = \frac{1-\alpha_t}{1-\alpha_{t-1}}\beta_t$. \mathbf{x}_{t-1} can be sampled as

$$\mathbf{x}_{t-1} = \mu_\theta(\mathbf{x}_t, t) + \sigma_t \varepsilon, \text{ with } \varepsilon \sim \mathcal{N}(0, I). \quad (9)$$

To train the diffusion model, the objective is to maximize the (log-) likelihood $\log p_\theta(\mathbf{x}_0) = \int p_\theta(\mathbf{x}_{0:T}) d\mathbf{x}_{1:T}$, which is computationally infeasible. Instead, we maximize the tractable variational lower bound of the log-likelihood. The loss function \mathcal{L} can be rewritten as

$$\begin{aligned} \mathcal{L}(\theta) = & \mathbb{E} \left[\underbrace{\mathcal{D}_{\text{KL}}(q(\mathbf{x}_T|\mathbf{x}_0)||p(\mathbf{x}_T))}_{\mathcal{L}_T} \right. \\ & \left. + \sum_{t=2}^T \underbrace{\mathcal{D}_{\text{KL}}(q(\mathbf{x}_{t-1}|\mathbf{x}_t, \mathbf{x}_0)||p_\theta(\mathbf{x}_{t-1}|\mathbf{x}_t))}_{\mathcal{L}_{t-1}} - \underbrace{\log p_\theta(\mathbf{x}_0|\mathbf{x}_1)}_{\mathcal{L}_0} \right], \quad (10) \end{aligned}$$

where $\mathcal{D}_{\text{KL}}(q || p)$ denotes the Kullback–Leibler (KL) divergence between two distributions q and p .

DiT architecture

To extend the continuous diffusion models to the text domain, we adopt the Diffusion-LM⁴⁵ framework that maps discrete text into a continuous latent space via an embedding function e_ϕ . The framework is then trained to jointly learn the diffusion model's parameters and word embeddings in an end-to-end manner. A detailed derivation of the end-to-end training objective is provided in Supplementary Section 3. To condition the model on a target, we adopt the classifier-free guidance approach⁴⁶. The model is trained to jointly learn both conditional and unconditional generation by randomly replacing the condition label \mathbf{c} with a learnable 'null' token \emptyset during training, with a fixed probability p_{drop} . This approach enables flexible control during inference by replacing the predicted noise ε_θ with a weighted combination of conditional and unconditional predictions as

$$\hat{\varepsilon}_\theta(\mathbf{x}_t, t, \mathbf{c}) = \omega \varepsilon_\theta(\mathbf{x}_t, t, \mathbf{c}) + (1 - \omega) \varepsilon_\theta(\mathbf{x}_t, t, \emptyset), \quad (11)$$

where $\omega \geq 1$ is the guidance weight that balances the influence of conditional scores, controlling the trade-off between generation performance and sampling diversity. Here $\varepsilon_\theta(\mathbf{x}_t, t, \mathbf{c})$ and $\varepsilon_\theta(\mathbf{x}_t, t, \emptyset)$ denote the predicted noise from the conditional and unconditional models, respectively. Note that our diffusion model is trained to directly predict \mathbf{x}_0 instead of noise. We can derive the noise predictions from the model output $f_\theta(\mathbf{x}_t, t)$ using equation (7) as $\varepsilon_\theta = (\mathbf{x}_t - \sqrt{\alpha_t} f_\theta(\mathbf{x}_t, t)) / \sqrt{1 - \alpha_t}$.

To learn the reverse process, we adopt a transformer architecture based on DiTs³⁸. Unlike traditional diffusion models that use convolutional networks, a DiT leverages self-attention to capture long-range dependencies and complex interactions, making it effective for high-dimensional, structured data. To incorporate conditional labels $\mathbf{c} \in \mathbb{R}^h$ into our model, we first project each value into the embedding space, using a (learnable) linear projection layer and yielding the condition embeddings $\mathbf{y} \in \mathbb{R}^d$. When multiple conditional properties are considered, each is processed by a separate projection layer and the resulting conditional embeddings are concatenated. The conditional information, processed through the projection layer, is then integrated into the denoising process of the transformer model via cross-attention

mechanisms⁴⁷, enabling the model to effectively capture interactions between input and conditional information. In addition, the conditional embeddings \mathbf{y} are projected and added to the time embedding t , which is then processed through an adaLN³⁸ to predict a series of parameters, including global scale and shift parameters γ and β , and dimension-wise scaling parameters α . The adaLN blocks adaptively modulate the feature activations, leveraging the conditional information, which has been shown to be effective in improving the model's generation performance³⁸. Besides the compressive response and linear elastic properties investigated in this paper, the framework can be readily extended to a broader range of target properties without architectural changes. We refer to the code ('Code availability' section) for technical details regarding our DiT architecture.

Machine learning protocols

The performance of the proposed generative framework depends on several key design and training choices. The dataset of 23,534 samples balances the computational cost of FE simulations with model performance; ablation studies on smaller subsets indicate diminishing gains with additional data, while the full dataset yields robust inverse design performance. The transformer architecture (including the number of attention heads, embedding dimension and transformer hidden dimension) and training hyperparameters (including optimizer, learning rate and noise schedule) were determined through systematic ablation studies, which reveal that model performance is robust across a range of hyperparameter choices. Detailed ablation experiments and the final model configuration are provided in Supplementary Section 4. To comprehensively assess the model's generation performance, we evaluate the distribution of generated design properties under both conditional and unconditional generation settings (Supplementary Section 6). The model demonstrates stable and reliable generation performance across various target properties, effectively leveraging the probabilistic nature of generative models to address the one-to-many mapping inherent to inverse design.

FE simulation

To extract the stress–strain response of constructed shell structures, FE simulations are conducted using the commercial software ABAQUS/CAE 2023. The base material of all structures is described by an elastic–plastic constitutive model, with parameters calibrated from experimental uniaxial tensile test data (see ref. 41 for material characterization details). Each structure is discretized using a finite-strain, three-node triangular shell element (S3R). A periodic mesh is generated to ensure compatibility with the imposed periodic boundary conditions. Mesh refinement studies yield sufficient convergence of the effective (homogenized) stress–strain response and the stress distribution at an element size of 0.2 mm, as presented in Supplementary Section 2. The shell unit cell is positioned between two rigid plates with periodic boundary conditions prescribed on all lateral surfaces. The bottom plate is fixed, and a compressive strain up to 30% is applied by displacing the top plate vertically down. General contact with a friction coefficient of 0.6 is applied to all interacting surfaces within the unit cell. To promote convergence and numerical stability throughout the large-deformation regime in the presence of buckling and contact, a dynamic implicit solver with moderate dissipation is used to extract the quasi-static response. We record displacements, stresses and reaction forces of nodes in contact with the upper rigid plate at 50 equidistant strain increments. To facilitate the machine learning model training, we reduce the dimensionality of the target by representing the stress–strain response as a vector $\boldsymbol{\sigma} \in \mathbb{R}^{11}$, which contains the compressive stress at 11 strategically selected strain levels across the applied strain range. We verify that the full stress–strain response can be accurately reconstructed via cubic spline interpolation of these sampled points (see Supplementary Section 2 for further details). To validate quasistatics, we

ensure that the kinetic energy remains below 1% of the internal energy at all strain increments. The effective stiffness tensor is computed via FE homogenization of a single unit cell with periodic boundary conditions, and the effective (anisotropic) Poisson's ratios are extracted at small strains. All simulations are performed on the Euler cluster of ETH Zurich.

Fabrication and experimental validation

Specimens tested in this work were fabricated using digital light synthesis with a Carbon M2 3D printer, operating at an average writing speed of 22 mm h⁻¹ and a layer thickness of 100 μm. The printing material is UMA 90 resin (Carbon, Inc.), a one-part photopolymer with a tensile modulus of 484 MPa, ultimate strength of 11.9 MPa and 19.3% elongation at break⁴¹. After printing, samples were first cleaned by immersion in isopropyl alcohol under orbital agitation for 5 min to remove excess resin, followed by ultraviolet postcuring for 3 min to ensure complete photopolymerization. To enable direct comparison across different shell topologies, the wall thickness of each design was scaled proportionally to maintain a consistent relative density of 10% for all specimens. Two rigid plates of thickness 1 mm are added at the top and bottom during 3D printing to facilitate a uniform load distribution during compression testing. Uniaxial displacement-controlled compression tests were conducted using an Instron 5943 Single Column testing machine at a quasi-static strain rate of 0.0005 s⁻¹. The effective strains and stresses were calculated from the recorded force-displacement data and measured sample dimensions. Load-displacement data were acquired at a sampling frequency of 10 Hz throughout the compression process.

Reporting summary

Further information on research design is available in the Nature Portfolio Reporting Summary linked to this article.

Data availability

The training and test dataset (consisting of implicit equations, their corresponding stress-strain responses and effective stiffness data) and the pretrained models are available in the ETHZ Research Collection⁵⁵.

Code availability

The complete source code for this work, including data generation, model training and the conditional generation of new metamaterial designs with target responses, is available via GitHub at <https://github.com/li-zhengz/DiffusionMetamaterials.git> and via Zenodo at <https://doi.org/10.5281/zenodo.18598195> (ref. 56).

References

- Surjadi, J. U. et al. Mechanical metamaterials and their engineering applications. *Adv. Eng. Mater.* **21**, 1800864 (2019).
- Jiao, P., Mueller, J., Raney, J. R., Zheng, X. & Alavi, A. H. Mechanical metamaterials and beyond. *Nat. Commun.* **14**, 6004 (2023).
- Han, S. C., Lee, J. W. & Kang, K. A new type of low density material: shellular. *Adv. Mater.* **27**, 5506–5511 (2015).
- Bonatti, C. & Mohr, D. Smooth-shell metamaterials of cubic symmetry: anisotropic elasticity, yield strength and specific energy absorption. *Acta Mater.* **164**, 301–321 (2019).
- Chen, X. et al. Light-weight shell-lattice metamaterials for mechanical shock absorption. *Int. J. Mech. Sci.* **169**, 105288 (2020).
- Wang, Y., Zeng, Q., Wang, J., Li, Y. & Fang, D. Inverse design of shell-based mechanical metamaterial with customized loading curves based on machine learning and genetic algorithm. *Comput. Methods Appl. Mech. Eng.* **401**, 115571 (2022).
- Meza, L. R., Das, S. & Greer, J. R. Strong, lightweight, and recoverable three-dimensional ceramic nanolattices. *Science* **345**, 1322–1326 (2014).
- Davami, K. et al. Ultralight shape-recovering plate mechanical metamaterials. *Nat. Commun.* **6**, 10019 (2015).
- Jung, G. S. & Buehler, M. J. Multiscale mechanics of triply periodic minimal surfaces of three-dimensional graphene foams. *Nano Lett.* **18**, 4845–4853 (2018).
- Iyer, J., Moore, T., Nguyen, D., Roy, P. & Stolaroff, J. Heat transfer and pressure drop characteristics of heat exchangers based on triply periodic minimal and periodic nodal surfaces. *Appl. Therm. Eng.* **209**, 118192 (2022).
- Liu, Y. et al. Ultrafast shape-reconfigurable chiral mechanical metamaterial based on prestressed bistable shells. *Adv. Funct. Mater.* **33**, 2300433 (2023).
- Abueidda, D. W. et al. Effective conductivities and elastic moduli of novel foams with triply periodic minimal surfaces. *Mech. Mater.* **95**, 102–115 (2016).
- Xia, L. & Breitkopf, P. Recent advances on topology optimization of multiscale nonlinear structures. *Arch. Comput. Methods Eng.* **24**, 227–249 (2017).
- Telgen, B., Sigmund, O. & Kochmann, D. M. Topology optimization of graded truss lattices based on on-the-fly homogenization. *J. Appl. Mech.* **89**, 061006 (2022).
- White, D. A., Arrighi, W. J., Kudo, J. & Watts, S. E. Multiscale topology optimization using neural network surrogate models. *Comput. Methods Appl. Mech. Eng.* **346**, 1118–1135 (2019).
- Zheng, L., Kumar, S. & Kochmann, D. M. Data-driven topology optimization of spinodoid metamaterials with seamlessly tunable anisotropy. *Comput. Methods Appl. Mech. Eng.* **383**, 113894 (2021).
- Kingma, D. P. & Welling, M. Auto-encoding variational Bayes. Preprint at <https://doi.org/10.48550/arXiv.1312.6114> (2013).
- Goodfellow, I. J. et al. Generative adversarial nets. *Adv. Neural Inf. Process. Syst.* **27**, 2672–2680 (2014).
- Fuhr, A. S. & Sumpster, B. G. Deep generative models for materials discovery and machine learning-accelerated innovation. *Front. Mater.* **9**, 865270 (2022).
- Bastek, J.-H., Kumar, S., Telgen, B., Glaesener, R. N. & Kochmann, D. M. Inverting the structure-property map of truss metamaterials by deep learning. *Proc. Natl. Acad. Sci. USA* **119**, e2111505119 (2022).
- Zheng, X., Chen, T.-T., Guo, X., Samitsu, S. & Watanabe, I. Controllable inverse design of auxetic metamaterials using deep learning. *Mater. Des.* **211**, 110178 (2021).
- Thakolkaran, P., Espinal, M., Dhulipala, S., Kumar, S. & Portela, C. M. Experiment-informed finite-strain inverse design of spinodal metamaterials. *Extrem. Mech. Lett.* **74**, 102274 (2025).
- Deng, B. et al. Inverse design of mechanical metamaterials with target nonlinear response via a neural accelerated evolution strategy. *Adv. Mater.* **34**, 2206238 (2022).
- Bastek, J.-H. & Kochmann, D. M. Inverse design of nonlinear mechanical metamaterials via video denoising diffusion models. *Nat. Mach. Intell.* **5**, 1466–1475 (2023).
- Kartashov, N. & Vlassis, N. N. A large language model and denoising diffusion framework for targeted design of microstructures with commands in natural language. *Comput. Methods Appl. Mech. Eng.* **437**, 117742 (2025).
- Kumar, S., Tan, S., Zheng, L. & Kochmann, D. M. Inverse-designed spinodoid metamaterials. *npj Comput. Mater.* **6**, 1–10 (2020).
- Ho, J., Jain, A. & Abbeel, P. Denoising diffusion probabilistic models. *Adv. Neural Inf. Process. Syst.* **33**, 6840 (2020).
- Rombach, R., Blattmann, A., Lorenz, D., Esser, P. & Ommer, B. High-resolution image synthesis with latent diffusion models. In *Proc. 2022 IEEE/CVF Conference on Computer Vision and Pattern Recognition (CVPR)* 10674–10685 (IEEE, 2022).
- Zeni, C. et al. A generative model for inorganic materials design. *Nature* **639**, 624–632 (2025).
- Watson, J. L. et al. De novo design of protein structure and function with RFdiffusion. *Nature* **620**, 1089–1100 (2023).

31. Vlassis, N. & Sun, W. Denoising diffusion algorithm for inverse design of microstructures with fine-tuned nonlinear material properties. *Comput. Methods Appl. Mech. Eng.* **413**, 116126 (2023).
32. Zheng, X., Shiomi, J. & Yamada, T. Optimizing metamaterial inverse design with 3D conditional diffusion model and data augmentation. *Adv. Mater. Technol.* **10**, 2500293 (2025).
33. Liu, Z. et al. MeshDiffusion: score-based generative 3D mesh modeling. In *Proc. 11th International Conference on Learning Representations (ICLR 2023)*.
34. Luo, S. & Hu, W. Diffusion probabilistic models for 3D point cloud generation. In *Proc. 2021 IEEE/CVF Conference on Computer Vision and Pattern Recognition (CVPR)* 2836–2844 (IEEE, 2021).
35. Al-Ketan, O. & Abu Al-Rub, R. K. Multifunctional mechanical metamaterials based on triply periodic minimal surface lattices. *Adv. Eng. Mater.* **21**, 1900524 (2019).
36. Udrescu, S.-M. & Tegmark, M. AI Feynman: a physics-inspired method for symbolic regression. *Sci. Adv.* **6**, eaay2631 (2020).
37. Jadhav, Y. et al. Generative lattice units with 3D diffusion for inverse design: GLU3D. *Adv. Funct. Mater.* **34**, 2404165 (2024).
38. Peebles, W. & Xie, S. Scalable diffusion models with transformers. In *Proc. 2023 IEEE/CVF International Conference on Computer Vision (ICCV)* 4172–4182 (IEEE, 2023).
39. Gandy, P. J., Bardhan, S., Mackay, A. L. & Klinowski, J. Nodal surface approximations to the P,G,D and I-WP triply periodic minimal surfaces. *Chem. Phys. Lett.* **336**, 187–195 (2001).
40. von Schnering, H. G. & Nesper, R. Nodal surfaces of Fourier series: fundamental invariants of structured matter. *Z. Phys. B Condens. Matter* **83**, 407–412 (1991).
41. Rosa, M. I. N., Karapiperis, K., Radi, K., Pesciulli, E. & Kochmann, D. M. Enhanced deformability through distributed buckling in stiff quasicrystalline architected materials. *Adv. Mater.* **37**, 2505125 (2025).
42. Amorim, D. J. N., Nachtigall, T. & Alonso, M. B. Exploring mechanical meta-material structures through personalised shoe sole design. In *Proc. ACM Symposium on Computational Fabrication* (ed. Spencer, S. N.) 1–8 (ACM, 2019).
43. Perroni-Scharf, M., Ferguson, Z., Buttrille, T., Portela, C. & Luković, M. K. Data-efficient discovery of hyperelastic TPMS metamaterials with extreme energy dissipation. In *Proc. Special Interest Group on Computer Graphics and Interactive Techniques Conference 1-12 (SIGGRAPH Conference Papers 2025)*.
44. Ronneberger, O., Fischer, P. & Brox, T. U-Net: convolutional networks for biomedical image segmentation. In *Proc. Medical Image Computing and Computer-Assisted Intervention – MICCAI 2015* (eds Navab, N. et al.) 234–241 (Springer International Publishing, 2015).
45. Li, X. L., Thickestun, J., Gulrajani, I., Liang, P. & Hashimoto, T. B. Diffusion-LM improves controllable text generation. *Advances in Neural Information Processing Systems* **35**, 4328–4343 (2022).
46. Ho, J. & Salimans, T. Classifier-free diffusion guidance. Preprint at <https://doi.org/10.48550/arXiv.2207.12598> (2022).
47. Vaswani, A. et al. Attention is all you need. In *Advances in Neural Information Processing Systems Vol. 30* (eds von Luxburg, U. et al.) 5998–6008 (2017).
48. Papadopoulos, I. P. A., Farrell, P. E. & Surowiec, T. M. Computing multiple solutions of topology optimization problems. *SIAM J. Sci. Comput.* **43**, A1555–A1582 (2021).
49. Bastek, J.-H., Sun, W. & Kochmann, D. M. Physics-informed diffusion models. In *Proc. 13th International Conference on Learning Representations (ICLR 2025)*.
50. Settles, B. *Active Learning Literature Survey. Technical Report* (Univ. Wisconsin-Madison Department of Computer Sciences, 2009).
51. Zheng, L., Karapiperis, K., Kumar, S. & Kochmann, D. M. Unifying the design space and optimizing linear and nonlinear truss metamaterials by generative modeling. *Nat. Commun.* **14**, 7563 (2023).
52. Li, J. et al. Inverse design of metamaterials with manufacturing-guiding spectrum-to-structure conditional diffusion model. *Cell Rep. Phys. Sci.* **7**, 103174 (2026).
53. Mirabolghasemi, A., Akbarzadeh, A. H., Rodrigue, D. & Theriault, D. Thermal conductivity of architected cellular metamaterials. *Acta Mater.* **174**, 61–80 (2019).
54. Park, J., Lee, Y. & Kim, J. Multi-modal conditional diffusion model using signed distance functions for metal-organic frameworks generation. *Nat. Commun.* **16**, 34 (2025).
55. Zheng, L. DiffuMeta: algebraic language models for inverse design of metamaterials via diffusion transformers: dataset and model checkpoints. *ETH Zurich Research Collection* <https://doi.org/10.3929/ethz-b-000746797> (2025).
56. Zheng, L. li-zhengz/DiffusionMetamaterials: initial release. *Zenodo* <https://doi.org/10.5281/zenodo.18598195> (2026).

Acknowledgements

We thank P. Thakolkaran for his early contributions that informed the development of the design space and the parameterization. This research received financial support from ETH Zurich through the ETH+ grant SynMatLab.

Author contributions

L.Z. was responsible for conceptualizing the project, developing the methodology, implementing the software and performing validation. L.Z. also curated and visualized the data, wrote the original draft and contributed to the review and editing process. S.K. and D.M.K. contributed to the conceptualization and methodology development, were involved in the review and editing of the paper, and provided overall supervision for the project.

Competing interests

The authors declare no competing interests.

Additional information

Supplementary information The online version contains supplementary material available at <https://doi.org/10.1038/s42256-026-01218-8>.

Correspondence and requests for materials should be addressed to Siddhant Kumar or Dennis M. Kochmann.

Peer review information *Nature Machine Intelligence* thanks Daniel Acuna Ramirez and the other, anonymous, reviewer(s) for their contribution to the peer review of this work.

Reprints and permissions information is available at www.nature.com/reprints.

Publisher's note Springer Nature remains neutral with regard to jurisdictional claims in published maps and institutional affiliations.

Springer Nature or its licensor (e.g. a society or other partner) holds exclusive rights to this article under a publishing agreement with the author(s) or other rightsholder(s); author self-archiving of the accepted manuscript version of this article is solely governed by the terms of such publishing agreement and applicable law.

© The Author(s), under exclusive licence to Springer Nature Limited 2026

Reporting Summary

Nature Portfolio wishes to improve the reproducibility of the work that we publish. This form provides structure for consistency and transparency in reporting. For further information on Nature Portfolio policies, see our [Editorial Policies](#) and the [Editorial Policy Checklist](#).

Statistics

For all statistical analyses, confirm that the following items are present in the figure legend, table legend, main text, or Methods section.

n/a Confirmed

- The exact sample size (n) for each experimental group/condition, given as a discrete number and unit of measurement
- A statement on whether measurements were taken from distinct samples or whether the same sample was measured repeatedly
- The statistical test(s) used AND whether they are one- or two-sided
Only common tests should be described solely by name; describe more complex techniques in the Methods section.
- A description of all covariates tested
- A description of any assumptions or corrections, such as tests of normality and adjustment for multiple comparisons
- A full description of the statistical parameters including central tendency (e.g. means) or other basic estimates (e.g. regression coefficient) AND variation (e.g. standard deviation) or associated estimates of uncertainty (e.g. confidence intervals)
- For null hypothesis testing, the test statistic (e.g. F , t , r) with confidence intervals, effect sizes, degrees of freedom and P value noted
Give P values as exact values whenever suitable.
- For Bayesian analysis, information on the choice of priors and Markov chain Monte Carlo settings
- For hierarchical and complex designs, identification of the appropriate level for tests and full reporting of outcomes
- Estimates of effect sizes (e.g. Cohen's d , Pearson's r), indicating how they were calculated

Our web collection on [statistics for biologists](#) contains articles on many of the points above.

Software and code

Policy information about [availability of computer code](#)

- Data collection
- Data analysis

For manuscripts utilizing custom algorithms or software that are central to the research but not yet described in published literature, software must be made available to editors and reviewers. We strongly encourage code deposition in a community repository (e.g. GitHub). See the Nature Portfolio [guidelines for submitting code & software](#) for further information.

Data

Policy information about [availability of data](#)

All manuscripts must include a [data availability statement](#). This statement should provide the following information, where applicable:

- Accession codes, unique identifiers, or web links for publicly available datasets
- A description of any restrictions on data availability
- For clinical datasets or third party data, please ensure that the statement adheres to our [policy](#)

All data needed to evaluate the conclusions in the paper are described in the paper and the Supplementary Information. The training and test dataset (consisting of implicit equations, their corresponding stress-strain responses, and effective stiffness data) and the pre-trained models are available in the ETHZ Research Collection at <https://doi.org/10.3929/ethz-b-000746797>.

Research involving human participants, their data, or biological material

Policy information about studies with [human participants or human data](#). See also policy information about [sex, gender \(identity/presentation\), and sexual orientation](#) and [race, ethnicity and racism](#).

Reporting on sex and gender	N/A
Reporting on race, ethnicity, or other socially relevant groupings	N/A
Population characteristics	N/A
Recruitment	N/A
Ethics oversight	N/A

Note that full information on the approval of the study protocol must also be provided in the manuscript.

Field-specific reporting

Please select the one below that is the best fit for your research. If you are not sure, read the appropriate sections before making your selection.

Life sciences Behavioural & social sciences Ecological, evolutionary & environmental sciences

For a reference copy of the document with all sections, see [nature.com/documents/nr-reporting-summary-flat.pdf](https://www.nature.com/documents/nr-reporting-summary-flat.pdf)

Life sciences study design

All studies must disclose on these points even when the disclosure is negative.

Sample size	Sample sizes were not predetermined; we used all available samples that met the predefined inclusion criteria and for which complete measurements were obtained. The sample sizes were sufficient for the analyses as evidenced by convergence of the model training and agreement between predicted and experimentally measured stress-strain behavior.
Data exclusions	No data points or samples were excluded from the analyses after data collection, and no exclusion criteria were applied.
Replication	Replicability and generalization of the method were demonstrated using independently fabricated samples representing different designs. The agreement between the predicted and experimentally measured mechanical responses across these distinct structures validates the methodology and supports the reliability of the reported results.
Randomization	Allocation into groups was not relevant to this study. The experiments consisted of mechanical testing of generated 3D-printed samples, and all successfully fabricated samples were measured.
Blinding	Blinding was not relevant to this study. The experiments consisted of mechanical testing of generated 3D-printed metamaterial samples, with data acquired automatically by the measurement apparatus. No group comparisons or subjective assessments involved.

Reporting for specific materials, systems and methods

We require information from authors about some types of materials, experimental systems and methods used in many studies. Here, indicate whether each material, system or method listed is relevant to your study. If you are not sure if a list item applies to your research, read the appropriate section before selecting a response.

Materials & experimental systems

n/a	Involved in the study
<input checked="" type="checkbox"/>	<input type="checkbox"/> Antibodies
<input checked="" type="checkbox"/>	<input type="checkbox"/> Eukaryotic cell lines
<input checked="" type="checkbox"/>	<input type="checkbox"/> Palaeontology and archaeology
<input checked="" type="checkbox"/>	<input type="checkbox"/> Animals and other organisms
<input checked="" type="checkbox"/>	<input type="checkbox"/> Clinical data
<input checked="" type="checkbox"/>	<input type="checkbox"/> Dual use research of concern
<input checked="" type="checkbox"/>	<input type="checkbox"/> Plants

Methods

n/a	Involved in the study
<input checked="" type="checkbox"/>	<input type="checkbox"/> ChIP-seq
<input checked="" type="checkbox"/>	<input type="checkbox"/> Flow cytometry
<input checked="" type="checkbox"/>	<input type="checkbox"/> MRI-based neuroimaging

Plants

Seed stocks

N/A

Novel plant genotypes

N/A

Authentication

N/A